ICARUS 73, 279–293 (1988)

# Equation of State of Ammonia–Water Liquid: Derivation and Planetological Applications[1]

S. K. CROFT, J. I. LUNINE, AND J. KARGEL

*Lunar and Planetary Laboratory, University of Arizona, Tucson, Arizona 85721*

Received May 4, 1987; revised August 31, 1987

**An equation of state for ammonia–water liquid has been calculated by least-squares fit for the following range of parameters: 0 to 100 wt% $NH_3$, 170 to 300°K, and 0 to 10 kb. Measured and calculated liquid densities were used in conjunction with solid density and thermodynamic measurements to estimate the thermal expansion and density at 1 bar for the solid phases of ammonia dihydrate, ammonia monohydrate, and ammonia hemihydrate between 0°K and their respective melting points. The peritectic ammonia–water liquid near pure ammonia dihydrate in composition was found to have a density of about 0.946 g/cm$^3$ and to be approximately neutrally buoyant relative to the corresponding solid phases. This implies that igneous activity involving ammonia–water liquids on icy satellites may be both extrusive and intrusive in nature, possibly giving rise to a wide variety of morphologic and tectonic forms.** 

## INTRODUCTION

The ammonia hydrates are plausible constituents of the icy satellites and comets, comprising as much as 10% of the total mass (Lewis 1972). They are of particular interest because the presence of ammonia in water ice lowers the melting point of a peritectic mixture (~33% by mass $NH_3$) to about 175°K (Rollet and Vuillard 1956). This melting temperature is low enough to be reached in the interiors of icy satellites only 500 to 1000 km in radius by radioactive heating alone, possibly accounting for the resurfacing observed on the satellites of Saturn and Uranus in this size range. In addition, the potentially significant mass fraction of ammonia hydrates in the interiors of the icy satellites indicates that information concerning the densities of these compounds at various temperatures and pressures is necessary for construction of accurate models of the satellites' interiors. Unfortunately, many of the physical properties of the ammonia hydrates and their associated liquids are poorly determined. We have therefore assembled the data available in the literature and initiated experimental and theoretical studies to derive the desired physical properties as far as is feasible. In this report, we present an equation of state (EOS) for ammonia–water liquid to determine liquid density as a function of composition, temperature, and pressure. We then apply our EOS (1) to obtain estimates of the densities of the ammonia hydrate solids at 1 bar as functions of temperature and (2) to begin investigation of the dynamics of ammonia–water volcanism on the icy satellites.

## THE LIQUID $NH_3$–$H_2O$ EQUATION OF STATE

*Data.* Density measurements over the full range (0.0 to 1.0) of the mass fraction $X$ of $NH_3$ in water solution between temperatures of 260 and 300°K were adopted from the international critical tables edited by Gillespie (1928). Density values for pure liquid $NH_3$ between 190 and 290°K were taken from Haar and Gallagher (1978). These data are shown in Fig. 1. Measure-

[1] Contribution No. 87-13 of the Theoretical Astrophysics Program, University of Arizona.



0019-1035/88 $3.00

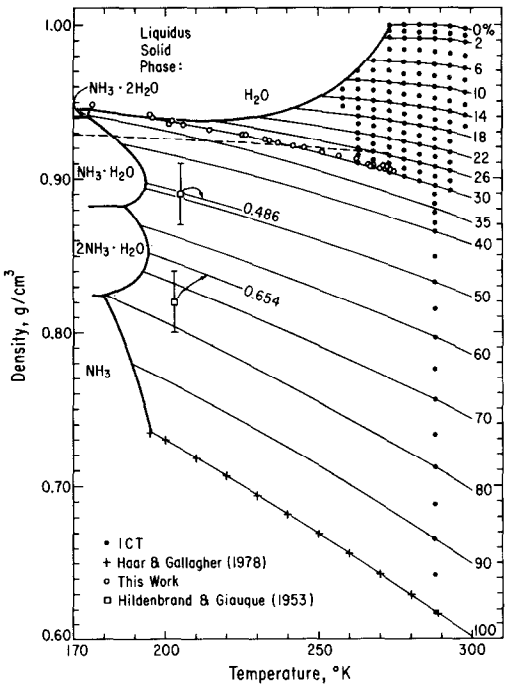


FIG. 1. Density–temperature–composition relations for liquid ammonia–water at 1 bar. Solid curves were calculated from Eqs. (2) and (3) for the mass% $NH_3$ values shown. All of the data points shown were used in the least-squares fit except the two points of Hildenbrand and Giauque (1953). The dashed line indicates the density of ice Ih.

ments at $X \leq 0.4$ are at atmospheric pressure. Measurements at larger values of $X$ at the upper end of our temperature range are confined against their own vapor pressure, a maximum of about 10 bars for pure $NH_3$ near 300°K.

The published data for liquid $NH_3$–$H_2O$ well characterize the densities of the pure end-members from about 300°K down to their respective freezing points, but only data relatively far from the freezing points were available for intermediate compositions ($X \gtrsim 0.2$) as may be seen in Fig. 1. Thus estimation of the densities of the congruent liquids of the ammonia hydrates at their respective melting points required considerable extrapolation. Extrapolation schemes were rendered uncertain by the well-known density inversion of $H_2O$ near freezing, but also by comparisons of the adopted International Critical Table (ICT) data and liquid $NH_3$–$H_2O$ density measurements by Sourirajan and Kennedy (1963). These latter data, while agreeing to within a few thousandths gram per cubic centimeter with the ICT data in absolute density, show systematic deviations in the volume coefficient of thermal expansion from the ICT data, as seen in Fig. 2. Therefore, we made a series of density runs near $X = 0.29$ from 300°K down to freezing near 190°K to resolve the ambiguity. Those measurements are described below. Since our thermal expansion data are consistent with extrapolations of the ICT data, we did not include the data of Sourirajan and Kennedy in our calculations at low pressure because of the apparent systematic deviations.

Density measurements at high pressure were adopted from Haar and Gallagher (1978) for pure $NH_3$ (0 to 5 kbar) and from Haar *et al.* (1984) for pure $H_2O$ (0 to 30 kbar). The only density measurements

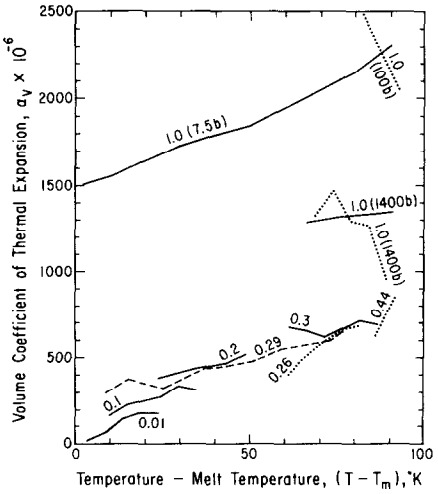


FIG. 2. Volume coefficient of thermal expansion of ammonia–water liquid for selected ammonia contents and temperatures. Solid lines are derived from the ICT data, dotted lines from Sourirajan and Kennedy (1963), and the dashed line from averages of the data in Table I. The Sourirajan and Kennedy data show large systematic differences from our data and the ICT data. The slight curvature of the individual composition curves prompted the parabolic form for $\alpha_V$ used in the least-squares solution.

above ambient pressure at intermediate compositions are those of Sourirajan and Kennedy (1963) (0 to 1.4 kbar). As mentioned above, Sourirajan and Kennedy's absolute densities agree within a few 10ths of a percent with densities from our other data sources. Also, the derived bulk moduli match those derived from the data of Haar and Gallagher (1978) and Haar *et al.* (1984) for the pure end-members to within a few percent. Thus the data of Sourirajan and Kennedy (1963) are used in the construction of the EOS at high pressure and intermediate compositions.

*Experimental measurements.* The density of commercially available analytical reagent grade ammonium hydroxide was determined by volumetric analysis for temperatures down to the peritectic freezing point. A graduated volumetric flask was filled with about 1015 ml of liquid at 273.15°K, which then was sealed. The density of the liquid at 273.15°K was adopted from the International Critical Tables (Gillespie 1928). The flask was cooled in various constant-temperature baths. Pressure effects on the density were deemed negligible as the pressure inside the sealed flask during each run began at 1 bar and decreased as the flask cooled. The temperature of the flask's contents was monitored using a chromel–alumel thermocouple inserted to the center of the flask. When thermal equilibrium in the flask was closely approached as determined by temperature measurements of the flask and the bath, the volume of the liquid was measured and then normalized to the volume at 273.15°K to yield the density as a function of temperature. Minor corrections were applied to account for the thermal expansion of the flask. The volume expansivity of the flask was determined by calculating the difference between the known density of water (from the ICT) and the measured density of water in the flask over the temperature range 273 to 363°K. The density differentials as a function of temperature, assumed to be due to expansion of the flask, yield a volume expansivity of about $6 \pm 1 \times 10^{-6}$ $°K^{-1}$. The density data for three experimental runs are given in Table I and are illustrated along with previously published data in Fig. 1. The first and third runs analyzed the densities of liquids with assays of 29.4 wt% $NH_3$, while the second run used a liq-

TABLE I

AMMONIUM HYDROXIDE DENSITY DATA

| Run No. 1 29.4 wt% $NH_3$ | | Run No. 2 28.9 wt% $NH_3$ | | Run No. 3 29.4 wt% $NH_3$ | |
|---|---|---|---|---|---|
| Temperature (°K) | Density (g $cm^{-3}$) | Temperature (°K) | Density (g $cm^{-3}$) | Temperature (°K) | Density (g $cm^{-3}$) |
| 273.2 | 0.9056 | 273.4 | 0.9069 | 274.1 | 0.9047 |
| 272.2 | 0.9059 | 272.6 | 0.9069 | 273.3 | 0.9056 |
| 271.8 | 0.9061 | 271.3 | 0.9082 | 267.9 | 0.9087 |
| 270.4 | 0.9066 | 262.6 | 0.9127 | 266.2 | 0.9093 |
| 267.0 | 0.9077 | 202.0 | 0.9384 | 241.7 | 0.9217 |
| 256.9 | 0.9149 | 196.8 | 0.9405 | 234.3 | 0.9249 |
| 251.3 | 0.9177 | 195.3 | 0.9419 | 232.9 | 0.9259 |
| 245.3 | 0.9201 | 195.0 | 0.9422 | 226.8 | 0.9284 |
| 237.0 | 0.9233 | 176.2 | 0.9484 | 225.4 | 0.9284 |
| 233.7 | 0.9246 | | | 214.5 | 0.9317 |
| | | | | 205.7 | 0.9348 |
| | | | | 201.4 | 0.9360 |

uid with 28.9 wt% $NH_3$. The formal uncertainty in the densities from all sources is $7 \times 10^{-4}$ g cm$^{-3}$ at the lower temperatures and somewhat less at higher temperatures.

*Form of EOS.* An equation of state of the following form was adopted:

$$\rho = \rho_r(T_r) \exp\left\{-\int_{T_r}^{T} \alpha_V \, dT\right\}\left[\frac{K_O' P}{K_O} + 1\right]^{1/K_O'}, \quad (1)$$

where $\rho_r(T_r)$ is a reference density at an arbitrary reference temperature $T_r$, $\alpha_V$ is the volume coefficient of thermal expansion, $K_O$ and $K_O'$ are, respectively, the bulk modulus and pressure derivative of the bulk modulus, $T$ is temperature, and $P$ is pressure. The portion of Eq. (1) in square brackets is the pressure term in the Murnaghan equation of state (Murnaghan 1944) obtained by integrating the relation $K = K_O + K_O'P$. The term in the exponential is simply the integral form of the definition of the volume coefficient of thermal expansion, $\alpha_V = -1/\rho(\partial\rho/\partial T)$.

## RESULTS

*Equation of state.* The numerical fit to Eq. (1) was done in two nearly independent steps: (1) a fit to $\rho_r(T_r)$ and the exponential thermal expansion term using only low-pressure density data and (2) a subsequent fit to the pressure term using bulk moduli derived from the high-pressure density data.

The low-pressure fit was obtained by least-squares (Bevington 1969) using 182 low-pressure points (Fig. 1). The derived expressions are

$$\rho(T, X, P = 0) = \rho_r(288.15°\text{K}) \exp\{a_1(T - 288.15) + a_2/2\,[(T - T_m)^2 - (288.15 - T_m)^2] + a_3/3\,[(T - T_m)^3 - (288.15 - T_m)^3, \quad (2a)$$

where

$$\rho_r(288.15°\text{K}) = 0.9991 - 0.4336X + 0.3303X^2 + 0.2833X^3 - 1.9716X^4 + 2.1396X^5 - 0.7294X^6 \quad (2b)$$

$$a_1 = -1.0 \times 10^{-6}(-92.88 + 1371.05X + 185.91X^2) \quad (2c)$$

$$a_2 = -1.0 \times 10^{-6}(14.51 - 47.50X + 42.35X^2) \quad (2d)$$

$$a_3 = -1.0 \times 10^{-6}(-0.0764 + 0.3118X - 0.2465X^2), \quad (2e)$$

and the melting point, $T_m$, fit piece-wise to the five sections of the $NH_3$–$H_2O$ liquidus (data from Rollet and Vuillard 1956, Gillespie 1928):

$$\text{for } X \le 0.329,\ T_m = 273.15 - 53.07X - 1651.4X^2 + 11{,}842X^3 - 46{,}269X^4 + 56{,}695X^5 \quad (3a)$$

$$0.329 < X \le 0.353,\ T_m = 184.7 - 29.17X \quad (3b)$$

$$0.353 < X \le 0.572,\ T_m = 248.07 - 1789.77X + 8585.6X^2 - 14479X^3 + 8064X^4 \quad (3c)$$

$$0.572 < X \le 0.803,\ T_m = -1435.42 + 7867.6X - 14{,}140X^2 + 11{,}357X^3 - 3524X^4 \quad (3d)$$

$$0.803 < X \le 1.0,\ T_m = 172.44 - 239.48X + 504.3X^2 - 241.7X^3. \quad (3e)$$

The liquidus solid phase for each expression is, in order of increasing $X$: $H_2O$ (Eq. (3a)), $NH_3 \cdot 2H_2O$ (Eq. (3b)), $NH_3 \cdot H_2O$ (Eq. (3c)), $2NH_3 \cdot H_2O$ (Eq. (3d)), and $NH_3$ (Eq. (3e)). Liquidus liquid phase densities and density isograms for selected compositions computed from Eq. (2) are shown in Fig. 1.

The fit to the pressure term in Eq. (1) was obtained by determining expressions for the bulk modulus, $K_O$, and its pressure derivative, $K_O'$. Because of the independence of the three data sets utilized, the fit consists of three parts: independent fits to $K_O$ and $K_O'$ for each of the pure end-members and an interpolation formula for intermediate compositions.

The expressions for $NH_3$ were obtained by least-squares fit to 70 density points se-

lected from Haar and Gallagher (1978) in the range of 195 to 400°K in temperature and 0 to 5 kbar in pressure, including the 11 low-pressure points indicated by crosses in Fig. 1. The results are

$$K_O = 48.503 \exp(-1.0134 \times 10^{-3} T^{1.3067})\text{kbar} \quad (4a)$$

$$K'_O = 4.0858 \times 10^{16} T^{-6.6083} + 4.1831. \quad (4b)$$

The expressions for $H_2O$ were obtained by least-squares fit to 50 density points selected from Haar *et al.* (1984) in the range of 273 to 400°K in temperature and 0 to 10 kbar in pressure, including points equivalent to the 6 points for pure $H_2O$ at 1 bar in Fig. 1. The results are

$$K_O = -73.184 + 0.5910T - 9.139 \times 10^{-4} T^2 \quad (4c)$$

$$K'_O = 39.999 - 0.2058T + 3.111 \times 10^{-4} T^2 \quad (4d)$$

The interpolation formula was obtained by comparison of the bulk moduli of $NH_3$ and $H_2O$ at 273, 283, and 298°K and the bulk moduli of three intermediate compositions ($X$ = 0.2565, 0.4365, and 0.718) obtained by least-squares fit to 69 selected density points from Sourirajan and Kennedy (1963) at the same temperatures. The 15 values of $K_O$ and $K'_O$ so derived are shown in Fig. 3. A cubic polynomial interpolation function was found to provide a reasonable fit. Because of the presumed greater accuracy of the end-member bulk moduli and because of apparent systematic differences of a few percent between the three data sets, the end points of the interpolation function were required to match the bulk moduli of $NH_3$ and $H_2O$ at each temperature. This determined two of the constants of the interpolation equation; the other two were determined by least-squares fit to the intermediate data points. Thus the final interpolation formula for $K_O$ is

$$K_O(X) = K_O(H_2O)(1 - X) + K_O(NH_3)X + C(X^2 - X) + D(X^3 - X), \quad (5a)$$

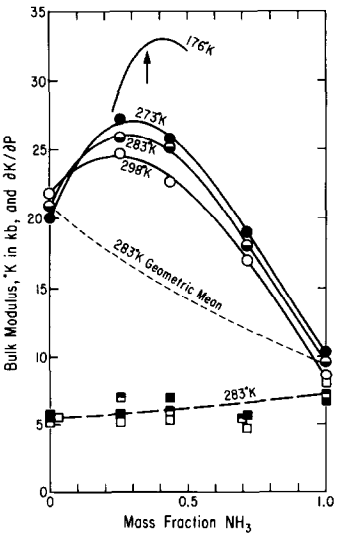


FIG. 3. Calculated bulk moduli (circles) and pressure derivative of the bulk moduli (squares) for ammonia–water liquid as a function of the ammonia mass fraction and temperature. Filled symbols are at 273°K, half-filled at 283°K, and open symbols at 298°K. The solid lines are a computed fit at the labeled temperatures to the bulk moduli. The heavy dashed line is a geometric mean fit to the pressure derivatives. The light dashed line is a geometric mean fit to the bulk moduli of the end-members only.

where

$$C = -638.89 + 1.9519T \quad (5b)$$

and

$$D = 316.84 - 0.99616T, \quad (5c)$$

where $K_O(NH_3)$ is calculated from Eq. (4a) and $K_O(H_2O)$ is calculated from Eq. (4c). The solid lines in Fig. 3 are calculated from Eqs. (5a)–(5c) for the temperatures shown. The fit is seen to be a reasonable one.

The values for $K'_O$ are also shown in Fig. 3. The scatter is considerable and shows no particular dependence on temperature. Thus a simple geometric mean (indicated by the heavy dashed line) was deemed sufficient for interpolation between the pure end-members:

$$K'_O(X) = [K'_O(NH_3)]^X K'_O(H_2O)^{1-X}, \quad (5d)$$

where $K'_O(NH_3)$ is determined from Eq.

(4b) and $K'_O(H_2O)$ is determined from Eq. (4d).

The equation of state of $NH_3$–$H_2O$ liquid as expressed by Eqs. (2) through (5) is admittedly a complex numerical recipe. The behavior modeled, however, is also complex. Our equation of state is comparable in complexity to the equation of state for pure $NH_3$ developed by Mills *et al.* (1984) and utilizes similar parameterizations. The forms and $P$, $T$, or $X$ dependencies of our parameterizations were determined solely by empirical analysis of the data and their peculiarities. A good example of these is the dependency of bulk modulus on composition and temperature illustrated in Fig. 3. Other parameterizations, such as that of Edwards *et al.* (1978) for the activity coefficient of ammonia–water liquid, were not used because they could not fit the data. Similarly, the number of significant figures retained in the empirical constants are the same as in the EOS of Mills *et al.* (1984) and are required for computation to match the accuracy of our data, which are given to four and five significant figures. Empirical parameterizations are used because derivation of the physical behavior of ammonia–water liquid from first principles, e.g., molecular dynamics, is a substantial challenge not within the scope of this paper. Simpler versions of our EOS were tried, including fewer terms in $\rho_r(T_r)$, constant and linear expressions in $T$ for $\alpha_V$, and fewer terms in the $K_O$ interpolation function, but the fits were markedly inferior to the current form. The liquidus temperature relations were convolved primarily because the inversion of the density curves at the water-rich end of the low-pressure data in Fig. 1 is related to the proximity of freezing. Normalization to the freezing curve yielded the approximate superposition of $\alpha_V$ for the various compositions seen in Fig. 2, resulting in fairly simple expressions for $\alpha_V$. Different convolutions are possible, but would almost certainly be of comparable complexity to obtain comparable accuracy.

The uncertainties in the densities computed from the EOS vary in different regions of $P$-$X$-$T$ space. The formal RMS uncertainty in the low-pressure calculation is only 0.0004 g/cm$^3$. Thus the fit is very good in the regions where data exist. The reliability of the interpolation into the large area in Fig. 1 where virtually no data exist is obviously problematical. The only measurements made prior to this report in the mid-range of ammonia content at low temperatures are the two points of Hildenbrand and Giauque (1953) shown in Fig. 1. The compositions for these two measurements are stoichiometric ammonia monohydrate and ammonia hemihydrate. The corresponding composition density curves calculated from Eqs. (2) and (3) are indicated by the arrows. The monohydrate point is well fit, but the calculated hemihydrate curve falls outside the experimental error bars. Hildenbrand and Giauque stated that their measurements were "rough," but the discrepancy remains. We note, however, the similar slopes of our data near $X = 0.29$ and that of the pure ammonia curve that bracket the region in question. If the hemihydrate point is correct, then a large negative anomaly in the thermal expansion must develop for $X$ between 0.3 and 0.6 that then becomes strongly positive for $X$ above 0.7 to match the observed pure ammonia curve. We deem this unlikely and suggest that the hemihydrate point is in error.

The formal errors in expressions for $K_O$ and $K'_O$ for $NH_3$ and $H_2O$ are all at the 5% level. The uncertainty in the interpolation for intermediate values of $X$ are seen in Fig. 3 to be near 5% also. For $NH_3$ this translates into a formal rms error of 0.004 g/cm$^3$ for the 70 high-pressure points. Thus where high-pressure data exist, the uncertainties in the densities are near 1%. The validity of extrapolation beyond the range of the data is difficult to assess because the derived equations are empirical interpolation functions. For example, the bulk modulus of the dihydrate congruent liquid near its freezing point is of interest. The arc in Fig. 3 labeled 176°K is an extrapolation calculated from

Eqs. 4 and 5. The computed arc is not inconsistent with a visual extrapolation of the existing data. The arrow indicates the dihydrate composition. The inferred bulk modulus of 32 kbar is similar to the measured $K_O$ for liquid $NH_3$ at its freezing point of 37 kbar and that for liquid $H_2O$ of 20 kbar. Thus the extrapolated liquid dihydrate bulk modulus is not unreasonable. However, direct measurements should eventually be made.

Our analysis of the data did indicate some features of physical interest. The bulk modulus data for intermediate compositions shown in Fig. 3 exhibit a substantial deviation from the values obtained by simple averaging techniques, such as is illustrated by the 283°K geometric mean curve. The maximum deviation from the simple average occurs near $X = 0.4$. The density data show a similar trend. Equation (2b) is a fit to the ICT data at 288.15°K, the only temperature at which density measurements over the entire range of ammonia–water compositions are available. The data used in determining Eq. (2b) are shown in Fig. 4. Also shown in Fig. 4 is the theoretical curve for the density, $\rho_{NI}$, calculated from the pure end-members assuming no interaction between the ammonia and water molecules:

$$\rho_{NI} = \left[\frac{1 - X}{\rho_{H_2O}} - \frac{X}{\rho_{NH_3}}\right]^{-1}.$$

The data show a substantial deviation from the noninteracting case, with densities being as much as 9% greater in the real mixtures, the maximum deviation again occurring near $X = 0.4$. Both data sets indicate significant molecular interactions resulting in a closer molecular packing in the mixed liquid than in either pure liquid. Edwards *et al.* (1978) also find deviations from simple mixing for the activity coefficient, although with a somewhat different dependence on composition. Thus accurate thermodynamic calculations involving ammonia–water mixtures should not rely on models which assume the adequacy of simple mixing of thermodynamic properties of pure water and ammonia.

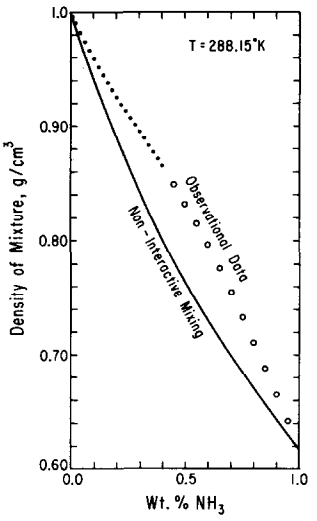


FIG. 4. Density of ammonia-water liquid at 288.15°K as a function of ammonia composition. Data points are from ICT and the solid line is the theoretical density curve of mixed compositions between ammonia and water assuming no molecular interactions. The large deviation implies a strong attraction between these two polarized molecules. The closed circles represent data at atmospheric pressure given to four significant figures. The open circles are data taken in closed tubes under the component's own vapor pressure and are given to only three significant figures.

## APPLICATIONS

*Solid ammonia hydrate densities at 1 bar.* In this section we derive estimates for the volume coefficient of thermal expansion, $\alpha_V$, and density, $\rho$, of each of the ammonia hydrates at 1 bar. We adopt the following form for the thermal expansion:

$$\alpha_V = AT^B, \tag{6}$$

from which the density is obtained by integration:

$$\rho = \rho_O \exp\left[-\frac{A}{B+1} T^{B+1}\right], \tag{7}$$

where $A$ and $B$ are empirical constants and $\rho_O$ is the density at 1 bar and absolute zero. Least-squares fits of Eqs. (6) and (7) to data for ice Ih and $NH_3$ I are given in Table II. The uncertainty in the fit to 20 ice density

TABLE II

EQUATIONS FOR DENSITY AND THERMAL EXPANSION OF THE $NH_3$–$H_2O$ SOLIDS

A. Volume coefficient of thermal expansion: $\alpha_V = AT^B$

| Compound | $A$ | $B$ | Notes |
|---|---|---|---|
| $H_2O$ | $2.437 \times 10^{-8}$ | 1.582 | Derived, 20 data points |
| $NH_3 \cdot 2H_2O$ | $2.239 \times 10^{-7}$ | 1.375 | Adopted |
| $NH_3 \cdot H_2O$ | $2.239 \times 10^{-7}$ | 1.375 | Derived, 2 data points |
| $2NH_3 \cdot H_2O$ | $2.239 \times 10^{-7}$ | 1.375 | Adopted |
| $NH_3$ | $0.93235 \times 10^{-6}$ | 1.2207 | Derived, 25 data points |

B. Density at 1 bar:

$$\rho = \rho_0 \exp\left[-\left(\frac{A}{B+1}\right) T^{B+1}\right]$$

| Compound | $\rho_0$ | $A/(B+1)$ | $B+1$ |
|---|---|---|---|
| $H_2O$ | 0.9338 ± 0.0008 | $9.438 \times 10^{-9}$ | 2.582 |
| $NH_3 \cdot 2H_2O$ | 0.9826 ± 0.0062 | $9.427 \times 10^{-8}$ | 2.375 |
| $NH_3 \cdot H_2O$ | 0.9588 ± 0.0031 | $9.427 \times 10^{-8}$ | 2.375 |
| $2NH_3 \cdot H_2O$ | 0.9364 ± 0.0100 | $9.427 \times 10^{-8}$ | 2.375 |
| $NH_3$ | 0.8659 ± 0.0020 | $4.198 \times 10^{-7}$ | 2.2207 |

values (Hobbs 1974, p. 348) is 0.0008 g/cm$^3$. The uncertainty in the fit to 20 $NH_3$ thermal expansion values (Manzhelii and Tolkachev 1966) and 5 $NH_3$ density points (Olovsson and Templeton 1959b, Tolkachev and Manzhelii 1966, Blum 1975) is also 0.0008 g/cm$^3$. Curves showing the density of solid $NH_3$ and $H_2O$ computed from Eq. (7) and the constants in Table II are shown in Fig. 5. Only the five $NH_3$ density points are shown for clarity. The other points (presumably smoothed data) would all fall within the thickness of the drawn curves. Thus the fits are seen to represent the data well.

The density data for the ammonia hydrate solids are much more limited. Only single X-ray diffraction measurements exist for the densities of each of the three ammonia hydrates: 0.9768 ± 0.0062 at 105°K for ammonia dihydrate ($NH_3 \cdot 2H_2O$, Bertie and Shehata 1984), 0.9520 ± 0.0031 at 113°K for ammonia monohydrate ($NH_3 \cdot H_2O$, Olovsson and Templeton 1959a), and 0.9171 ± 0.0100 g/cm$^{-3}$ at 178°K for ammonia hemihydrate ($2NH_3 \cdot H_2O$, Siemons and Templeton 1954). These data are shown in

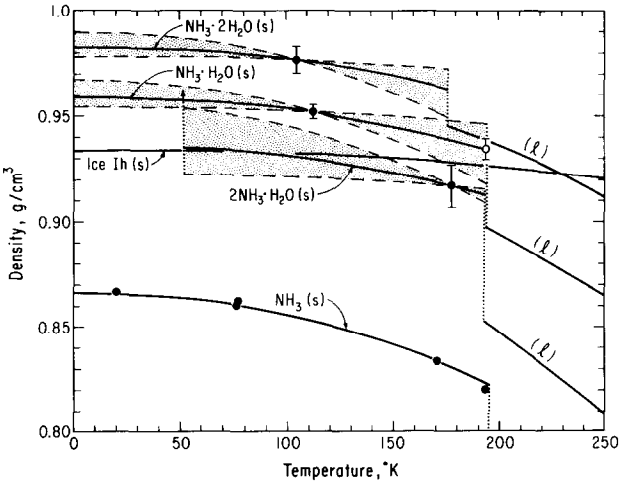


FIG. 5. Density–temperature curves for the five ammonia–water solids at 1 bar. Solid lines are least-squares fits to various data sets (see text and Table II). Dashed lines are approximate limits to the ammonia hydrate densities assuming thermal expansions for water ice (smaller thermal expansion) and solid ammonia (larger thermal expansion). Closed circles are measured points; the open circle is the calculated point given in Table III. Subscript "s" refers to solid state, "l" refers to liquid.

TABLE III

AMMONIA–WATER HYDRATE PHASE CHANGE SUMMARY

| Compound | $H_2O$ | $NH_3 \cdot 2H_2O$ | $NH_3 \cdot H_2O$ | $2NH_3 \cdot H_2O$ | $NH_3$ |
|---|---|---|---|---|---|
| Molecular weight | 18.01534 | 53.0613 | 35.0460 | 52.0766 | 17.03061 |
| Mass fraction $NH_3$ | 0.00 | 0.3210 | 0.4860 | 0.6541 | 1.0 |
| Melt temp. at 1 bar, °K | 273.15 | 176.16[a] | 194.15[b] | 194.32[b] | 195.36[c] |
| Latent heat of fusion, J/g | 333.5[d] | 131.9[a] | 187.2[b] | 189.0[b] | 322.2[c] |
| $dT/dP\|_{melt}$, °K/kbar | −7.38[e] | $2.59^{+1.37}_{-1.95}$ | 4.60 ± 0.60[f] | 8.00 ± 0.43 | 8.387[g] |
| $\delta V$ cm³/g $\equiv \frac{L}{T_m}\frac{dT}{dP}\|_m$ | −0.09011 | — | 0.0444 ±0.0058 | — | 0.1383 |
| $\delta V$ cm³/g $\equiv V_l - V_s$ | −0.09069 | 0.0191 | — | 0.0778 | 0.1464 |
| $\rho_l$ ($T_m$) | 0.99983[h] | 0.9454[i] | 0.8973[i] | 0.8521[i] | 0.7342[i] |
| $\rho_s$ ($T_m$) | 0.91671 ±0.00005[k] | 0.9628 +0.0097 −0.0133[l] | 0.9345 ±0.0051[m] | 0.9126 ±0.0035[l] | 0.8226[j] |

[a] Chan and Giauque (1964).
[b] Hildenbrand and Giauque (1953).
[c] Overstreet and Giauque (1937).
[d] Hobbs (1974, p. 362).
[e] Hobbs (1974, p. 351).
[f] Johnson *et al.* (1985).
[g] Mills *et al.* (1982).
[h] Harr *et al.* (1984).
[i] Eq. (3), at the appropriate stoichiometric compositions.
[j] $NH_3$(s) EOS, Table 2.
[k] Hobbs (1974, p. 346).
[l] Calculated assuming $\alpha_V$ of $NH_3 \cdot H_2O$(s). Error bars represent densities calculated assuming $\alpha_V$ of $H_2O$(s) and $NH_3$(s).
[m] The uncertainty in this density is derived from the estimated uncertainty in the Clapeyron slope.

Fig. 5 along with the respective congruent liquid density curves calculated from Eqs. (2) and (3). A second density point for $NH_3 \cdot H_2O$ at the melting point may be obtained from the calculated liquid density for the congruent liquid and other available thermodynamic data using a form of the Clausius–Clapeyron equation:

$$\frac{1}{\rho_l} - \frac{1}{\rho_s} \equiv \delta V = \frac{L}{MT_m}\frac{dT}{dP}\Big|_m, \qquad (8)$$

where $\rho_l$ and $\rho_s$ are, respectively, the liquid and solid densities at the melting temperature, $T_m$, $\delta V$ is the volume difference at $T_m$, $M$ is the molecular weight, $L$ is the latent heat of fusion, and $dT/dP|_m$ is the Clapeyron slope at melting. The appropriate thermodynamic data for each of the five $NH_3$–$H_2O$ compounds at melting are given in Table III. A complete set of experimental data is available for pure $H_2O$ and $NH_3$, allowing a comparison between the values for $\delta V$ computed from the observed densities (left-hand term in Eq. (8)) and the thermodynamic data (right-hand term in Eq. (8)). The percentage difference in the $\delta V$'s is about 0.6% for $H_2O$ and 5.8% for the $NH_3$, giving an idea of the uncertainties involved. The thermodynamic data for $NH_3 \cdot H_2O$ are used to obtain a solid density at melting of 0.9345 ± 0.0051 g/cm³, shown in Fig. 5. The two dashed curves shown in Fig. 5 for $NH_3 \cdot H_2O$ are derived by applying the equations of thermal expansion for ice Ih and $NH_3$ I to the single observed density point for $NH_3 \cdot H_2O$. The calculated melting point density for $NH_3 \cdot H_2O$ is seen to fall near the mean of the densities ob-

tained by extrapolation using the $H_2O$ and $NH_3$ ice thermal expansions. Thus the thermal expansion of $NH_3 \cdot H_2O$, intermediate between that of solid $H_2O$ and $NH_3$, appears to approximate the behavior of a simple mixture. However, the uncertainty in our calculated value is ≈30% of the difference between the two dashed curves at melting; thus deviations from simple mixing on the order of the deviation in the density data (Fig. 4) may be found by future direct measurements of $\alpha_V$ for $NH_3 \cdot H_2O$. The two monohydrate density values allow computation of two of the three constants in Eqs. (6) and (7), given the third. Lacking the data for a more precise interpolation, we adopt a geometric mean for the exponent $B$ for $NH_3 \cdot H_2O$ in Eq. (6) between the $B$ values for ice Ih and $NH_3$ and derive $A$ and $\rho_O$ from the density data. The results are given in Table II, and shown by the solid line in Fig. 5.

A similar procedure cannot be carried out for the dihydrate and monohydrate because their Clapeyron slopes at atmospheric pressure have not been directly measured (although a slope for the dihydrate using high-pressure data has been estimated; see below). We therefore adopt the thermal expansion derived for $NH_3 \cdot H_2O$ for the other two ammonia hydrates, as indicated in Table II, and derive $\rho_O$ for each from the observed densities. The resulting density curves are shown in Fig. 5, bracketed in each case by dashed curves representing extrapolations obtained by adopting the ice Ih and $NH_3$ I thermal expansions, which should in each case represent reasonable uncertainty limits. The hemihydrate curve cuts off at 54°K because of a solid-state phase change indicated at that temperature in the heat capacity data of Hildenbrand and Giauque (1953) similar to low-temperature phase changes seen in solid $CH_4$, $N_2$, and CO. Estimates for the Clapeyron slopes at 1 bar for the dihydrate and hemihydrate may now be obtained by working back from the adopted solid density curves, the calculated liquid density curves, and the thermodynamic data in Table III. This we have done, with the results given in Table III. The upper and lower uncertainties in the slopes are derived, respectively, from the solid densities calculated from the ice Ih and $NH_3$ I thermal expansions.

We emphasize that the Clapeyron slopes for the dihydrate and hemihydrate in Table III are based entirely on the thermodynamic data in the table and on the solid and liquid densities at atmospheric pressure computed from the equations derived in this report. However, a Clapeyron slope of ≈15°K/kbar is derived for the dihydrate from the melting point at one bar and the melting point near 8 kbar inferred by Johnson *et al.* (1985) and Johnson and Nicol (1987). This is substantially larger than the ≈2°K/kbar determined here. We maintain that the slope inferred from the high-pressure data cannot apply down to atmospheric pressure, because, given the thermodynamic data in Table III and the experimentally determined densities of a near-dihydrate liquid, a Clapeyron slope of 15°K/kbar yields a solid density for the dihydrate at one atmosphere and 176°K of 1.05 g/cm$^3$, a density clearly incompatible with the X-ray diffraction density of the dihydrate found by Bertie and Shehata (1984) seen in Fig. 5. We therefore suggest that the dihydrate phase inferred by Johnson *et al.* (1985) is not the same as that seen at 1 bar, but may be a high-pressure phase discussed in detail in the next section.

The calculated di- and hemihydrate Clapeyron slopes are shown in Fig. 6 along with the measured slopes of the monohydrate $H_2O$ and $NH_3$ as a function of the ammonia mass fraction. We note that the slopes exhibit a consistent functional dependence on the ammonia mass fraction, a property possibly shared by the $MgO$–$SiO_2$ system (Deer *et al.* 1971, p. 199, Bottinga and Richet 1978, Cox *et al.* 1979, Chapt. 3), a system which bears several other striking similarities to the $NH_3$–$H_2O$ system.

We recognize the large uncertainties in

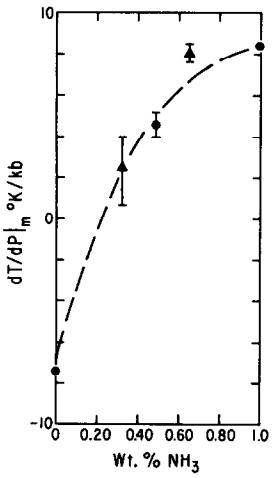


FIG. 6. Clapeyron slope at 1 bar for the five ammonia–water solids as functions of ammonia weight fraction. Dots are measured values; triangles are calculated from thermodynamic properties and calculated liquid and solid densities.

our derived and adopted relations in Table II. The leanness of the data base points up the need for further measurements. However, the density relations given in Table II are based on the presently available data and are presented in the spirit of reasonable approximations necessary for preliminary examination of the consequences of including the ammonia hydrates in models of the icy satellites.

*High-pressure phase diagram of ammonia–water system.* In this section we apply our results on the volume of the liquid ammonia–water solution to interpret the high-pressure data of Johnson and Nicol (1987). In particular, we will show that the dihydrate phase they identified at high pressure must be significantly denser than the low-pressure dihydrate solid if it is to satisfy thermodynamic constraints. In presenting our calculations we caution the reader that the Johnson and Nicol high-pressure data are currently under dispute; the possibility has been raised that dihydrate is not the stable solid phase at moderate (30%) ammonia concentrations and ≈10 kbar pressure (Nicol 1987, personal communication). The analysis detailed below is intended to demonstrate by example the utility of our low-pressure results in interpreting data on the phase diagram at high pressure. If dihydrate is ultimately found not to be a stable high-pressure phase, the results of this section will also need revision, but the analytic technique will be the same.

The congruent melting point of dihydrate as a function of pressure is given by integrating the differential form of the Clausius–Clapeyron relationship:

$$T(P) - T(P_0) \equiv T - T_0 = \frac{\delta V}{\delta S}(P - P_0),$$

where $\delta S$, $\delta V$ are the entropy and volume change in going from the dihydrate solid to a liquid of congruent composition and $P_0$ is the reference or starting pressure. We assume the entropy change is that given by Chan and Giauque (1964), $4 \times 10^8$ ergs/mole/°K, for transition from low-pressure dihydrate to the liquid at 176°K. The volume of the liquid at higher pressures is calculated using two alternative equations of state: (a) The equation of state derived above (Eq. (1)), for a 66% water liquid, is

$$V_l(P\text{kbar}, T°K) = 53/\Big\{0.8889 \exp[-3.6638 \times 10^{-4} q - 1.81315 \times 10^{-6} q^2 + 5.7060 \times 10^{-10} q^3 + 6.03979 \times 10^{-2}]\Big[\frac{K_0'}{K_0} P + 1\Big]^{1/K_0'}\Big\}, \quad (9)$$

where $q = T - 179.61$ and $K_0$ and $K_0'$ are calculated from Eqs. (5a) and (5d) for $X = 0.321$. (b) The equation of state for liquid water from Lupo and Lewis (1979) is multiplied by a numerical factor to yield the correct liquid volume at 1 bar (56.1 $cm^3$/mole; see Table III):

$$V_l = 56.0 \times \Big\{[1.0014 + q \cdot 3.4 \times 10^{-4} + q^2 \cdot 8.6 \times 10^{-7} - P/22.4 + P \cdot 3.4 \times 10^{-2} \exp\Big[\frac{-3.4}{P}\Big]\Big\}.$$

The volume of the dihydrate solid is parameterized in the form

$$V_s = V_0 \exp(-\kappa P + \alpha q),$$

where $\kappa$ = compressibility, $\alpha$ = thermal expansion coefficient, and $V_0$ = volume of the solid at 1 bar. Initially, the compressibility and thermal expansion coefficients were treated as constant adjustable parameters; as explained below, better results are obtained with $\alpha$ a function of temperature and $\kappa$ a function of pressure.

Figure 7 shows the congruent melting curve for dihydrate assuming a volume of the solid at 1 bar and 176°K of 54.7 cm$^3$/mole, as calculated from X-ray diffraction data by Bertie and Shehata (1984). Also shown are constraints based upon the data of Johnson *et al.* (1985) and Johnson and Nicol (1987). These include a congruent melting point of 294°K at 8 kbar and a congruent melting range of 250 to 270°K in the pessure regime 1.4 to 4.2 kbar. The latter is based upon observed melting of the dihydrate to a liquid composition of 20% ammonia at 2.8 ± 1.4 kbar by Johnson and Nicol (1987). The congruent melting temperature must be equal to, or higher than, the observed point.

Figure 7 shows that neither data constraint can be met by a dihydrate solid with the specified volume from low-pressure structural studies, for reasonable solid thermal expansion and compressibility coefficients (i.e., we exclude a compressibility for the solid greater than that for the liquid). An alternative possibility, that the entropy change at higher pressures is much smaller than the one measured by Chan and Giauque (1964), is unlikely since the value required is so small that the solid would have to be a glass. We assume in the analysis presented here that the dihydrate solid seen at high pressure by Johnson *et al.* (1985) and Johnson and Nicol (1987) is a high-density polymorph of the low-pressure phase, in analogy with structural changes in water ice solid phases. This allows us to choose the volume of the solid at the solid–

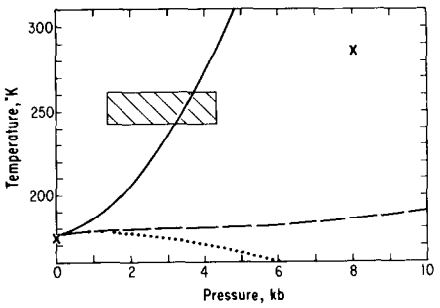


FIG. 7. Congruent melting curve of ammonia dihydrate assuming a single solid phase from 1 to 10,000 bars. For the solid line, $\kappa = 10^{-4}$ bar$^{-1}$, $\alpha = 10^{-6}$ °K$^{-1}$; for the dashed line, $\kappa = 10^{-5}$ bar$^{-1}$, $\alpha = 10^{-5}$ °K$^{-1}$; for the dotted line, $\kappa = 10^{-6}$ bar$^{-1}$, $\alpha = 10^{-5}$ °K$^{-1}$. The volume of the solid at 1 bar is taken to be 54.7 cm$^3$/mole; the liquid equation of state derived in the text is used. X's and box denote constraints from data of Johnson and Nicol (1987), and the low-pressure congruent melting point estimated to be 177°K.

solid phase transition to be a free parameter. We choose this transition to be at 1 kbar, which is roughly where the melting curve for the low-pressure dihydrate solid becomes horizontal ($dT/dP = 0$) for reasonable values of $\kappa(\leq 10^{-5}$ bar$^{-1})$. In the water ice system, the first high-pressure transition is at 2 kbar (Eisenberg and Kauzmann 1969). A transition pressure higher than 1 kbar for the dihydrate would require a volume change from the low- to the high-pressure solid phase larger than that calculated below.

Figure 8 shows melting curves assuming a solid–solid transition at 1 kbar and the liquid volume given by Eq. (9), for several values of $V_0'$ (the solid volume at 1 kbar), $\kappa$, and $\alpha$. The curve in the 2- to 4-kbar region, where the first data constraint is located, is most sensitive to the choice of $V_0'$. The shape of the curve at 8 kbars depends largely upon the choice of thermal expansion and compressibility coefficients. A value of $\kappa$ greater than $10^{-4}$ bar$^{-1}$ or less than $10^{-6}$ bar$^{-1}$ is probably unreasonable based upon data for other water and ammonia solids (see above, and Lupo and Lewis 1979). Likewise, the value of $\alpha$ is constrained to be within $\approx 10^{-3}$ to $10^{-4}$ °K$^{-1}$.

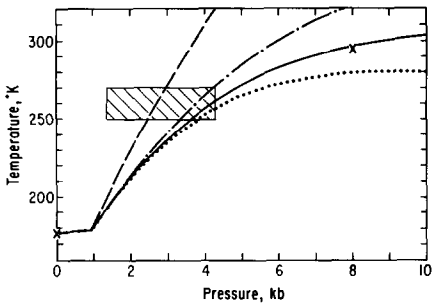


FIG. 8. Same as Fig. 7, assuming a solid–solid phase transition at 1 kbar. For the solid line, $\kappa = 10^{-5}$ bar$^{-1}$, $\alpha = 2 \times 10^{-3}$ °K$^{-1}$, and $V'_0 = 41.0$ cm$^3$/mole, where $V'_0$ is the volume of the high-pressure dihydrate phase at 1 kbar; for the dashed line, $\kappa = 10^{-6}$ bar$^{-1}$, $\alpha = 10^{-3}$ °K$^{-1}$, $V'_0 = 35.0$ cm$^3$/mole; for the dotted line, $\kappa = 10^{-6}$ bar$^{-1}$, $\alpha = 2 \times 10^{-3}$ °K$^{-1}$, $V'_0 = 41.0$ cm$^3$/mole; for the dot–dashed line, $\kappa = 10^{-6}$ bar$^{-1}$, $\alpha = 10^{-3}$ °K$^{-1}$, $V'_0 = 41.0$ cm$^3$/mole.

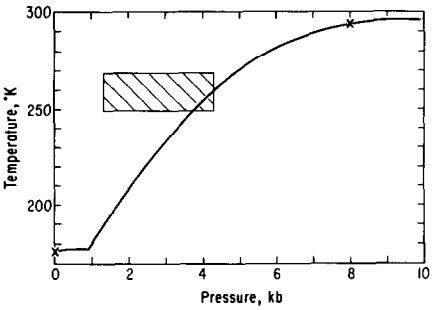


FIG. 9. Same as Fig. 8, but for a thermal expansion coefficient varying with temperature and a compressibility varying with pressure. The parameters were chosen to best fit the data constraints and are given in the text.

Within this rather large range, an acceptable fit to the Johnson and Nicol (1987) data requires a large value of $\alpha$.

A plausible modification based upon the behavior of other ices is a temperature-dependent $\alpha$. We chose the form

$$\alpha = A + B\left(1 - \exp\left[-\frac{T}{T_a} + 1\right]\right).$$

We also select a pressure-dependent $\kappa$:

$$\kappa = C - D\left(1 - \exp\left[\frac{10^3 - P(\text{bars})}{P_a}\right]\right).$$

Figure 9 shows the resulting best fit to the Johnson and Nicol data, with $V'_0 = 43$ cm$^3$/mole, $A = 3 \times 10^{-4}$ °K$^{-1}$, $B = 2.5 \times 10^{-3}$ °K$^{-1}$, $C = 1 \times 10^{-5}$ bar$^{-1}$, $D = 9.0 \times 10^{-6}$ bar$^{-1}$, $P_a = 10{,}000$ bars, $T_a = 179$°K, and Eq. (9). The modified Lupo and Lewis equation of state requires a somewhat larger solid thermal expansion coefficient and a somewhat smaller (by ~5%) $V'_0$ to fit the Johnson and Nicol data. All of the physical parameters listed above are reasonable based upon the values for other ammonia–water and water ice phases. In fitting the Johnson and Nicol data, the curve in Fig. 9 passes through 260°K at 4.3 kbar, rather than at 2.8 kbar. In view of their error bars, this fit is acceptable. A steeper melting curve (passing through 260°K at a lower pressure) would require a larger volume jump between solid phases at 1 kbar and less plausible compressibility and thermal expansion parameters to bend the curve over to fit the Johnson and Nicol data at 8 kbar.

Figure 10 plots solid and liquid volumes for the congruent melting curve of Fig. 9.The solid density at 1 kbar is 1.23 g/cm$^3$, a 27% increase over the low-pressure dihydrate. This is somewhat larger than the density constrasts among water ice polymorphs (Eisenberg and Kauzmann 1969). We have assumed a single phase from 1 to 10 kbars. A piecewise fit with several new dihydrate phases is also possible and suggested by the fact that water ice changes phase three times along its melting curve in that pressure regime. However, the John-

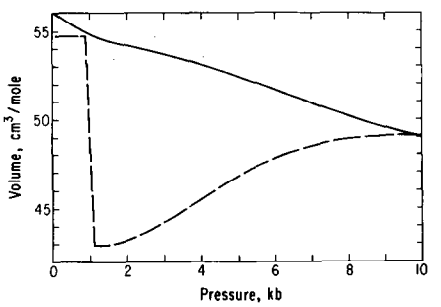


FIG. 10. Molar volumes of solid (dashed line) and liquid (solid line) dihydrate phases for the congruent melting curve given in Fig. 9.

son and Nicol data do not allow us to distinguish between these possibilities.

*Solid–liquid density contrast and ammonia–water volcanism.* In this section we briefly consider some of the possible implications for ammonia–water volcanism on small icy satellites indicated by the liquid ammonia–water densities. Since we are considering only the smaller satellites, this discussion is based entirely on the low-pressure data. The density of the ammonia–water peritectic liquid at melting (~175°K) is about 0.946 g/cm$^3$. In an undifferentiated icy satellite with typical densities near 1.3 g/cm$^3$ or larger, the peritectic liquid should have no problem reaching the surface. Thus on small satellites where the interior temperatures reach 175°K only over a small volume near the center, limited areas of surface flooding would be expected, probably confined to preexisting depressions as the maria basalts are on the Moon (Wood 1973). In larger satellites where the peritectic melting point is reached over large fractions of the interior, enough peritectic melt is generated (based on cosmic abundance estimates) to bury the original surfaces under a layer of ammonia hydrate solids several tens of kilometers thick. Consequently, late-arriving liquids must penetrate a thick ammonia hydrate layer to continue to reach the surface. If the surface $NH_3$–$H_2O$ layers consist of ice Ih and ammonia monohydrate as suggested by Lunine and Stevenson (1985), then the density at 60°K (appropriate to the Uranian satellites) is about 0.945 g/cm$^3$ and about 0.936 g/cm$^3$ at melting. If equilibrium compositions are obtained, the surface layer would consist of a mixture of ammonia monohydrate and ammonia dihydrate with a density of 0.980 g/cm$^3$ at 60°K and 0.962 g/cm$^3$ at melting. In either case, the peritectic liquid is nearly neutrally buoyant relative to the solid. A few percent porosity in the uppermost kilometer or two could prevent any liquid from reaching the surface.

The condition of near neutral buoyancy for ammonia–water melt in a fairly thick ice–ammonia hydrate crust provides some interesting morphological possibilities. Much of the later igneous activity may be primarily plutonic, producing limited surface flooding but possibly extensive surface tectonics such as groove-like structures due to dike swarms or the formation of magma chambers. If large magma chambers form, continued fractionation of the melt is possible under certain conditions, allowing the formation of a wide range of magma compositions, which, because of the strong dependence of viscosity of ammonia–water mixtures on composition (Kargel 1987), could give rise to a wide variety of surface flow morphologies. In addition, magmas reaching the surface may be partly congealed, thus possessing very large viscosities and thereby capable of forming very thick flows such as those seen on Ariel (Smith *et al.* 1986). Johnson and Nicol (1987) have considered the implications of dihydrate near-neutral buoyancy in Titan's interior.

These density considerations thus indicate mechanisms for producing volcanic and tectonic structures by ammonia–water volcanism in addition to those proposed by Stevenson (1982), particularly for the case of volcanism in a thick water ice–ammonia hydrate crust. We note also that the density relationships derived here will alter several details in a geological and oceanographical scenario for planets with ammonia water oceans presented by Foward (1984).

## ACKNOWLEDGMENTS

This work was supported by NASA Grants NSG741 (SKC, JK) and NAGW 1039 (JIL).

## REFERENCES

BERTIE, J. E., AND M. R. SHEHATA 1984. Ammonia dihydrate: Preparation, X-ray powder diffraction pattern and infrared spectrum of $NH_3 \cdot 2H_2O$ at 100K. *J. Chem. Phys.* **81,** 27–30.

BEVINGTON, P. R. 1969. *Data reduction and error analysis for the physical sciences.* McGraw–Hill, New York.

BLUM, A. 1975. Crystalline character of transparent solid ammonia. *Radiat. Eff.* **24,** 277–279.

BOTTINGA, Y., AND P. RICHET 1978. Thermodynamics of liquid silicates, a preliminary report. *Earth Planet. Sci. Lett.* **40,** 382–400.

CHAN, J. P., AND W. F. GIAUQUE 1964. The entropy of $NH_3 \cdot 2H_2O$ heat capacity from 15 to 300K. *J. Phys. Chem.* **68,** 3053–3057 (Erratum, 3912).

COX, K. G., J. D. BELL, AND R. J. PANKHURST 1979. *The Interpretation of Igneous Rocks.* Allen & Unwin, London.

DEER, W. A., R. A. HOWIE, AND J. ZUSSMAN 1971. *Rock Forming Minerals, Framework Silicates,* Vol. 4. Longman, London.

DORSEY, N. E. 1940. *Properties of Ordinary Water-Substance.* Reinhold, New York.

EDWARDS, T. J., J. NEWMAN, AND J. M. PRAUSNITZ 1978. Thermodynamics of vapor–liquid equilibria for the ammonia–water system. *Ind. Eng. Chem. Fundam.* **17,** 264–269.

EISENBERG, D., AND W. KAUZMANN 1969. *The Structure and Properties of Water.* Oxford Univ. Press, London/New York.

FOWARD, R. L. 1984. *The Flight of the Dragonfly.* Simon & Schuster, New York.

GILLESPIE, L. J. (Ed.) 1928. Density and thermal expansion of aqueous solutions of inorganic substances and strong electrolytes. In International Critical Tables, Vol. 3, p. 59.

HAAR, L., AND J. S. GALLAGHER 1978. Thermodynamic properties of ammonia. *J. Phys. Chem. Ref. Data* **7,** 635–792.

HAAR, L., J. S. GALLAGHER, AND G. S. KELL 1984. *NBS/NRC Steam Tables.* Hemisphere Pub., Washington, DC.

HILDENBRAND, D. L., AND W. F. GIAUQUE 1953. Ammonium oxide and ammonium hydroxide. Heat capacities and thermodynamic properties from 15 to 300°. *J. Amer. Chem. Soc.* **75,** 2811–2818.

HOBBS, P. V. 1974. *Ice Physics.* Oxford Univ. Press (Clarendon), London/New York.

JOHNSON, M. L., AND M. NICOL 1987. The ammonia–water phase diagram and its implications for icy satellites. *J. Geophys. Res.* **92,** 6339–6349.

JOHNSON, M. L., A. SCHWAKE, AND M. NICOL 1985. Partial phase diagram for the system $NH_3$–$H_2O$: The water-rich region. In *Ices in the Solar System* (J. Klinger *et al.,* Eds.), p. 39–47. Reidel, Dordrecht.

KARGEL, J. S. 1987. Density and viscosity measurements of ammonia–water liquids. *Lunar Planet. Sci. XVIII,* 475–476. The Lunar and Planetary Institute, Houston.

LEWIS, J. S. 1972. Low temperature condensation from the solar nebula. *Icarus* **16,** 241–252.

LUNINE, J. I., AND D. J. STEVENSON 1985. Thermodynamics of clathrate hydrate at low and high pressures with application to the outer Solar System. *Astrophys. J. Suppl. Ser.* **58,** 493–531.

LUPO, M. J., AND J. S. LEWIS 1979. Mass–radius relationships in icy satellites. *Icarus* **40,** 157–170.

MANZHELII, V. G., AND A. M. TOLKACHEV 1966. Thermal expansion of crystalline ammonia. *Sov. Phys. Solid State* **8,** 827–830.

MILLS, R. L., D. H. LIEBENBERG, AND PH. PRUZAN 1982. Phase diagram and transition properties of condensed ammonia to 10kb. *J. Phys. Chem.* **86,** 5219–5222.

MILLS, R. L., D. H. LIEBENBERG, R. LESAR, AND PH. PRUZAN 1984. Equation of state of fluid $NH_3$ from P-V-T and ultrasound measurements to 12 kb. In *High Pressure in Science and Technology, Proc. 9th AIRAPT Int. High Press. Conf.* (C. Homan, R. K. MacCrone, and E. Whalley, Eds.), Part 2, pp. 43–50. North-Holland, New York.

MURNAGHAN, E. D. 1944. The compressibility of media under extreme pressures. *Proc. Natl. Acad. Sci.* **30,** 244–247.

OLOVSSON, I., AND D. H. TEMPLETON 1959a. The crystal structure of ammonia monohydrate. *Acta Crystall.* **12,** 827–832.

OLOVSSON, I., AND D. H. TEMPLETON 1959b. X-ray study of solid ammonia. *Acta Crystall.* **12,** 832–836.

OVERSTREET, R. AND W. F. GIAUQUE 1937. Ammonia. The heat capacity and vapor pressure of solid and liquid. Heat of vaporization. The entropy values from thermal and spectral data. *J. Amer. Chem. Soc.* **59,** 254–259.

ROLLET, A.-P., AND G. VUILLARD 1956. Sur un novel hydrate de l'ammoniac. *C.R. Acad. Sci. Paris* **243,** 383–386.

SIEMONS, W. J., AND D. H. TEMPLETON 1954. The crystal structure of ammonium oxide. *Acta Crystall.* **7,** 194–198.

SMITH, B. A., AND THE VOYAGER IMAGING TEAM 1986. Voyager 2 in the Uranian system: Imaging science results. *Science* **233,** 43–64.

SOURIRAJAN, S., AND G. C. KENNEDY 1963. Specific volumes of liquid ammonia–water mixtures in the temperature range 0° to 25° and pressure range 100 to 1400 bars. *J. Geophys. Res.* **68,** 4149–4155.

STEVENSON, J. D. 1982. Volcanism and igneous processes in small icy satellites. *Nature* **298,** 142–144.

TOLKACHEV, A. M., AND V. G. MANZHELII 1966. Density of solidified gases. *Sov. Phys. Solid State* **7,** 1711–1713.

WOOD, J. A. 1973. Bombardment as a cause of the lunar asymmetry. *Moon* **8,** 73–103.